Paper submitted to the NURETH-7 Conference,
Saratoga Springs, NY, September 10-15, 1995

Validation of the THIRMAL-1 Melt-Water Interaction Code*

by

C. C. Chu, J. J. Sienicki, and B. W. Spencer

Engineering Development Laboratories
Reactor Engineering Division
Argonne National Laboratory

May 1995

*Work sponsored by the United States Department of Energy Advanced Reactor Severe Accident Program.

Validation of the THIRMAL-1 Melt-Water Interaction Code

by

C. C. Chu, J. J. Sienicki, and B. W. Spencer
Argonne National Laboratory
9700 S. Cass Avenue
Argonne, Illinois 60439
(708) 252-6564

ABSTRACT

The THIRMAL-1 computer code has been used to calculate nonexplosive LWR melt-water interactions both in-vessel and ex-vessel. To support the application of the code and enhance its acceptability, THIRMAL-1 has been compared with available data from two of the ongoing FARO experiments at Ispra and two of the Corium Coolant Mixing (CCM) experiments performed at Argonne. THIRMAL-1 calculations for the FARO Scoping Test and Quenching Test 2 as well as the CCM-5 and -6 experiments were found to be in excellent agreement with the experiment results. This lends confidence to the modeling that has been incorporated in the code describing melt stream breakup due to the growth of both Kelvin-Helmholtz and large wave instabilities, the sizes of droplets formed, multiphase flow and heat transfer in the mixing zone surrounding and below the melt stream, as well as hydrogen generation due to oxidation of the melt metallic phase. As part of the analysis of the FARO tests, a mechanistic model was developed to calculate the prefragmentation as it may have occurred when melt relocated from the release vessel to the water surface and the model was compared with the relevant data from FARO.

1. INTRODUCTION

1.1 Background

The assessment of severe accident sequences in the light water reactors includes many situations in which molten core materials are released into water. In many instances the core materials enter the water in the form of a coherent melt stream. The THIRMAL-1 code has been developed at Argonne National Laboratory to provide an analysis tool for melt stream-water interactions in light water reactor severe accidents. The physical models and user's guide of THIRMAL-1 code have recently been comprehensively documented in a two-volume report prepared for the Electric Power Research Institute [1,2]. THIRMAL-1 is an outgrowth of an earlier code called THIRMAL-0 developed at Argonne [3]. In contrast to this earlier code, THIRMAL-1 incorporates significantly improved modeling and models for many additional processes. The THIRMAL-1 computer code is being used in the DOE Advanced Reactor Severe Accident Program and has been applied in studies of accident management for Swedish BWRs [4]. To support the

use of the code and assure its acceptability, it has been compared with available data from the FARO Scoping Test and Quenching Test 2 performed at elevated pressure and reported in the literature [5] as well as data from the Argonne Corium-Coolant Mixing (CCM) experiment at near atmospheric pressure conditions [6].

1.2 Brief Review of THIRMAL-1 Code

THIRMAL-1 was conceived and developed with a close connection to the behavior observed in and the understanding obtained from both simulant material and reactor material experiments. The simulant material tests of Spencer et. al. [7,8] showed the leading edge of the melt stream to be deformed and stripped after penetrating into the water pool and small melt droplets and ligaments to be stripped off of the melt stream column surface by the surrounding fluid. In the video and x-ray photographs from the simulant experiments of Schneider et. al. [9], an upward flowing vapor chimney can be observed surrounding the melt stream that undergoes sinuous or varicose deformation along its length while small drops and ligaments are observed to be stripped from the surface of the stream. Accordingly, THIRMAL-1 models erosion by stripping (i.e., small wave Kelvin-Helmholtz instabilities) from the stream surface, stripping from the leading edge surface, as well as breakup from large waves along the stream column. The mechanistic THIRMAL-1 approach thus reflects results from experiments with actual streams; this important aspect of the real premixing problem has instead been treated parametrically in the prefragmentation/cloud of spheres approach, an alternative premixing model [10]. Other modeling approaches on this subject have been developed. A description of the mechanism of the stripping at the stream column due to shear flow produced waves based on the Miles formulation of the instability has been given by Bürger et. al. [11]. Breakup of a melt stream due to Taylor instabilities alone at the leading edge of a melt stream has been described by Chu and Corradini [12].

THIRMAL-1 treats the case of a circular melt stream entering the water pool with a time varying diameter, velocity, temperature, and composition. Except for the initial transient penetration of the melt stream into the pool, the dominant fragmentation mechanism in the model is the erosion of molten droplets from the surface of the melt stream due to the formation of Kelvin-Helmholtz instabilities along the stream surface (Figures 1 and 2). Immediately behind the stream leading edge, the instabilities are driven by the upward flow of vapor inside a vapor film immediately surrounding the stream along part of its length. As the eroded fragments enter the surrounding water, heat transfer from the fragments gives rise to the local formation of steam which rises through the pool. This results in the formation of an interaction zone surrounding the stream containing melt droplets, melt particles, water, and steam. The radial extent of the interaction zone reflects the lateral migration of the droplets and particles and their temperatures that directly determine the vapor source.

Near the leading edge, the steam rises through water within the interaction zone in a bubbly flow regime. At increasing heights above the leading edge, the accumulation of steam increases the superficial vapor velocity through the interaction zone causing a transition to a churn turbulent flow regime. Dispersed flow typically develops in

the overlying part of the interaction zone. Here, melt droplets and particles together with water droplets are dispersed in the upward flowing steam. Heat transfer from the melt droplets and particles in the dispersed flow region typically produces superheated steam that exits the interaction zone at the elevation of the top of the pool.

Interactions of the upward flowing steam with the melt stream also result in the erosion of droplets from the stream surface through the Kelvin-Helmholtz instability mechanism. Heat transfer to the water droplets and the water at the outer boundary of the interaction zone can occur at such a high rate in the upper part of the dispersed flow region that local steam condensation is effectively eliminated. Depending upon the droplet/particle diameter and the vapor flow conditions, melt droplets and particles in the dispersed region may be swept up out of the pool or may settle downward through a continuous vapor flow before encountering the continuous liquid churn turbulent and bubbly flow regions near the stream leading edge.

In addition to Kelvin-Helmholtz instabilities, erosion of the melt stream leading edge due to boundary layer stripping is modeled as the stream initially penetrates downward rapidly through the water pool. Subsequently, the effects of erosion and acceleration of the melt stream cause the local stream diameter immediately behind at the leading edge to decrease to sizes so small that the stream column breaks up from capillary effects. In THIRMAL-1, this happens when the unstable large waves (i.e., varicose and sinuous wave growth) locally increase to about the melt stream radius. A number of relatively large melt fragments will be formed from the front part of the melt stream. Further breakup of the fragmented large segments is calculated according to a Weber number-based criterion.

2. COMPARISON WITH FARO EXPERIMENTS

2.1 General Description of FARO Tests

In the Scoping Test (ST) and Quenching Test 2 (QT2) (Table 1), 18 and 44 Kilograms, respectively, of an 80 wt % UO_2 - 20 wt % ZrO_2 melt were delivered under gravity through a 10 centimeter diameter nozzle into 0.87 and 1.0 meter depth pools, respectively, of slightly subcooled water [5]. It is noted that the Scoping Test is designated as L-06 and Quenching Test 2 as L-08 in recent publications. A feature of the FARO data is that the interaction vessel pressure increases before the onset of melt/water contact (MWC). According to the experimenters, the pressure increase observed in the Scoping Test during this period resulted from heating of the cover gas mixture above the water by the melt and from steam generation due to the "deequilibrium" at the time of pressure equilibration [5]. The Quenching Test 2 pressure increase is said to have been due only to gas heating [5]. Angelini, Yuen and Theofanous [10] claim that the pressurization rate of the gas before MWC in the Scoping Test can be explained by radiative heat transfer. As a test of this hypothesis, they note that breakup of the melt stream into drops of 1.2 centimeter diameter would afford sufficient additional surface area to provide the required heating.

TABLE 1. Comparison of the THIRMAL-1 Code with the Results of the FARO Scoping and Quenching Test 2

FARO Test Conditions	Scoping Test (ST)	Quenching Test 2 (QT2)
Mass, Kg	18	44
Melt composition, wt %	80% UO_2 + 20% ZrO_2	80% UO_2 + 20% ZrO_2
Delivery nozzle, cm	10	10
Free fall distance in cover gas, m	1.83	1.70
Water pool depth, m Initial water temperature, K	0.87 539 (water surface) 503 (bottom plate)	1.0 536 (water surface) 528 (bottom plate)
Gas Composition, mole %	91.5 steam + 8.5 Ar	84 steam + 16 Ar
Gas volume, m^3	0.464	0.875
Temperature at onset of melt release, K	543	536
Pressure at onset of melt release, MPa	5.0	5.8
Pressure at melt/water contact (MWC), MPa	5.4	6.1

Summary of Prefragmentation Analysis	Scoping Test	Quenching Test 2
Eroded melt mass before melt/water contact, Kg	4.9	9
Total eroded melt mass before all melt in water, Kg	8.8	19.7
Eroded melt droplet diameter, mm	5.5	3.83
Melt stream velocity at water surface, m/s	6.2	6.67
Melt stream diameter at water surface, cm	3.4	4.8
Pressure at MWC, MPa	5.2	6.06
Argon-steam mixture temperature at MWC, K	554	547

Comparison of THIRMAL-1 Predictions and Experiment Results	Experiment	Prediction	Experiment	Prediction
Corium collection conditions, wt % particles/droplets/stream	67/0/33	50/17[a]/33	68/0/32	46/22[a]/32
Fragmented mass, Kg	12.0	12.0	30.0	30.0
Unfragmented mass, Kg	6.0	6.0	14.0	14.0
Particle size range, mm	0.4 to 6.0	0.7 to 5.5	0.4 to 6.0	0.7 to 3.8
Median particle size, mm	4.5	5.0	3.8	3.8
Melt and bottom plate contact after melt/water contact, s	0.370	0.370	0.270	0.288
Mean velocity of melt in water, m/s	2.3	2.3	3.7	3.5
Pressure increase from MWC to end of fragmentation, MPa	0.7	0.7	1.5	1.5
Peak pressure increase rate, MPa/s	1.6	1.7	3.3	3.4
Equilibrium gas space temperature, K	582	579	578	607

a) Includes partially frozen droplets.

The assumption of complete breakup of all the released melt into 1.2 centimeter diameter spheres prior to melt-water contact is, however, not the only possible interpretation of the early pressure increase. The FARO experiments do not provide for any visualization of the melt relocation and melt-water interactions. Consequently, the actual state of the released melt is not observed. In the present analysis, it is shown below that an alternative explanation of the data can be obtained with a mechanistic model that calculates partial fragmentation of the released melt stream in the cover gas space such that the melt enters the water mainly in the form of a reduced thickness stream surrounded by melt drops eroded from the stream. Thus, the model does not assume a prior complete breakup of the released melt into drops.

2.2 Analysis of Melt Prefragmentation in the FARO Tests

Using the measured melt stream fall time and the free fall distance through the cover gas space, the velocity of the melt stream exiting from the release vessel nozzle is estimated. The measured melt stream fall time, t_{fall}, is estimated from experimental determination of the mean melt velocity in the cover gas and the free fall distance in the cover gas. The released melt stream is assumed to have the configuration of a segment of a cone as illustrated in Figure 3.

The single feature of the FARO tests that most promotes prefragmentation is the high pressure that exceeds 5 Megapascals. The high pressures are accompanied by high densities in the cover gas space that result in significant interactions of the falling melt stream with the gas. At the high gas space density, the initial disturbances on the melt stream surface will grow to a critical wave magnitude due to the Kelvin-Helmholtz instability within a fraction of a second as the melt stream falls through the gas phase. Subsequently, melt on the stream surface will be eroded away and the melt stream diameter will decrease with time. The melt erosion rate can be represented by [1]

$$\dot{M}_E = \frac{A_J'}{3}\left(\frac{\alpha_{max}}{k_{max}}\right)\rho_m \tag{1}$$

where

$$k_{max} = \frac{2\,\rho_f\,U_J^2}{3\,\sigma_m}, \tag{2}$$

$$\alpha_{max} = \frac{2\,(\rho_f)^{3/2}\,U_J^3}{\sqrt{27}\,\rho_m^{1/2}\,\sigma_m}, \tag{3}$$

The erosion rate represented by Eqs. (1 through 3) assumes that the gas phase interacting with the melt stream has a density at the film temperature. The melt mass cumulatively eroded with time before MWC is given by the equation,

$$\Delta M_E = \frac{(\rho_f \rho_m)^{\frac{1}{2}}}{\sqrt{27}} \int_{t_o}^{t} \int_{x_o}^{x_1} D_J U_J \, dx \, dt. \tag{4}$$

In the current analysis, the melt stream velocity and diameter are approximated by representative average values to obtain

$$\Delta M_E = \frac{(\rho_f \rho_m)^{\frac{1}{2}}}{\sqrt{27}} \overline{U}_J \overline{D}_J \int_{t_o}^{t} (x_1 - x_0) \, dt. \tag{5}$$

If the fall distance at the trailing edge of the melt stream, x_2, is greater than x_o, then x_2 should be used instead of x_o in Eq. (5).

In THIRMAL-1, the droplet diameter resulting from Kelvin-Helmholtz instability-induced erosion is equal to 1.5 times the inverse wavenumber of the fastest growing wavelength. Therefore, the corresponding increase with time of the eroded melt droplet surface area is calculated from the equation,

$$A_p(t) = \int \dot{A}_p \, dt = \frac{4 \rho_f}{\sigma_m C_o \sqrt{27}} \left(\frac{\rho_f}{\rho_m} \right)^{\frac{1}{2}} \int_{t_o}^{t} \int_{x_o}^{x_1} D_J U_J^3 \, dx \, dt, \tag{6}$$

where C_o is a constant equal to 1.5. Using the representative average melt stream velocity and diameter, the melt surface area is calculated from

$$A_p(t) = \frac{6}{\sqrt{27} \overline{D}_p} \left(\frac{\rho_f}{\rho_m} \right)^{\frac{1}{2}} \overline{U}_J \overline{D}_J \int_{t_o}^{t} (x_1 - x_0) \, dt, \tag{7}$$

where

$$\overline{D}_p = \frac{3 C_o \sigma_m}{2 \rho_f \overline{U}_J^2}. \tag{8}$$

The inception of melt erosion due to Kelvin-Helmholtz instability occurs when the initial disturbance on the melt surface, η_o, grows to the critical unstable wave magnitude expressed by the equation,

$$\eta(t) = \eta_o e^{\alpha t_o} \geq \frac{\lambda_{max}}{4} = \frac{\pi}{2 k_{max}}, \tag{9}$$

where

$$\alpha t_o = \int_o^{t_o} \left(\frac{\rho_f k^2}{\rho_m} U_J^2 - \frac{\sigma_m}{\rho_m} k^3 \right)^{\frac{1}{2}} dt, \tag{10}$$

Combining Eqs. (9 and 10), the minimum melt stream velocity at which the initial disturbances will grow to the critical unstable wave magnitude is given by

$$\ln (a/\eta_o) + \ln \left(\frac{\pi}{2ka} \right) - \frac{k}{2g} \sqrt{\frac{\rho_f}{\rho_m}} \left[U_{J.min} \left(U_{J.min}^2 - \frac{\sigma_m}{\rho_f} k \right)^{\frac{1}{2}} \right.$$

$$\left. - \frac{\sigma_m}{\rho_f} \log \left(U_{J.min} + \left(U_{J.min}^2 - \frac{\sigma_m}{\rho_f} k \right)^{\frac{1}{2}} \right) \right]_0^{t_o} = 0. \tag{11}$$

In Ref. [13], a value of $\ln (a/\eta_o) = 6.0$ characterizing the magnitude of initial disturbance was evaluated both from the slope of the stream length curve at low velocities and by extrapolating the wave node amplitude back to the nozzle. This value is assumed here.

Heating of the steam-gas mixture in the gas space is mainly caused by radiative heat transfer from the melt stream plus both radiative and forced convection heat transfer from the melt droplets to the gas phase mixture. The melt droplet heat transfer rate is thus

$$Q_p'' = C_{rad} h_{rad} (T_m - T_{sat}) + h_{conv} (T_m - T_g). \tag{12}$$

and the melt stream heat transfer rate is

$$Q_J'' = C_{rad} h_{rad} (T_m - T_{sat}). \tag{13}$$

The melt stream prefragmentation model (Eqs. (1) through (11)) are applied until $x_2 = H_{fall}$ to provide the conditions (e.g., melt stream diameter, velocity, mass, eroded melt droplet diameter, velocity, and mass) with which melt enters the water pool in the following THIRMAL-1 calculations. The gas-steam space heatup model (Eqs. (12) and (13)) are only used to calculate heating of steam-gas mixture in the gas space before the melt stream contacts the water (i.e., $x_1 = H_{fall}$).

The cover gas heatup rate is dependent upon the fraction of the energy radiated from the melt that is absorbed by the gas-steam mixture instead of the surrounding wall. Transmission and absorption of thermal radiation were analyzed by Condiff [14] in conjunction with the direct containment heating problem for pressurized water reactors. Results for the percent absorption in an infinite steam atmosphere at a pressure of 0.3 Megapascal for UO_2 at various temperatures were calculated using the exponential band model of Tien [15]. Since absorption depends upon the quantity of steam that the thermal radiation passes through, Condiff [16] suggested that the results calculated can be used in the present analysis through the use of a scaling relationship that accounts for the effects of the differences in pressure and distance between FARO and the containment conditions of Ref. [14]. In particular, he suggested that a length in

the FARO system be multiplied by the ratio of the steam partial pressure in FARO to 0.3 Megapascal in order to determine the corresponding distance. In the FARO test vessel, radiation reaching the surrounding wall will be reflected from the wall. Part of the reflected radiation will be absorbed in the steam prior to reflecting off of the wall again and so on. It follows that the fraction absorbed in the steam is given by an infinite series of terms. A simple estimate for a one-dimensional long cylinder is

$$C_{rad} = 1 - \frac{\epsilon_w (1 - F)}{1 - (1 - F)^2 (1 - \epsilon_w)}. \qquad (14)$$

Taking the absorbed fraction in an infinite medium to be 0.25 and assuming a wall emittance for steel of 0.3, it is found that about 60 percent of the radiation is absorbed in the steam. However, because this simple estimate neglects the effects of the multiple droplets/particles existing in the cover gas and radiation out the top and bottom of the cylindrical volume, it is assumed that a smaller portion of 40 percent is absorbed by the steam.

For the conditions of the cover gas region where steam-gas mixture and melt droplets/particles are present, the energy radiated from the melt and absorbed in the steam-gas/melt optical thickness can be expressed as [17]

$$F' = 1.0 - \exp[-(a_g + a_m)L_m]. \qquad (15)$$

It is further assumed that the absorption fraction in an infinite medium gas-steam mixture is [17]

$$F = 1.0 - \exp[-a_g L_m] \qquad (16)$$

Using F' instead of F in Eq. (14) and assuming 9 Kilograms of melt droplets/particles with a drop diameter of 5.5 millimeters existing in the cover gas, it is found that a higher fraction of 75 percent of the radiation is absorbed in the gas-steam/melt optical thickness, but a lower fraction of 45 percent of the radiation is absorbed in the gas-steam mixture only. This further supports the use of a 40 percent absorption fraction in the steam.

The radiant energy not absorbed by the gas-steam mixture is assumed to be absorbed by the water through the surface of the water pool and to generate steam if the water temperature at the water surface is equal to the saturation temperature. This assumption clearly overestimates the steam production from the mechanism since the absorption of energy by the steel wall is neglected.

The melt stream prefragmentation/gas-steam space heatup model was applied to both the Scoping Test and Quenching Test 2 (Table 1). For the Scoping Test, the calculated gas mixture temperature rises only from 543 to 544.5 degrees Kelvin during the first 0.3 second but rises quickly from 544.5 to 554 degrees Kelvin by 0.46 second (MWC). The distribution of the mixture temperature for Scoping Test is shown in Figure 8 of Reference 8. It is observed that the measured gas space temperatures don't increase during the first 0.3 second but begin to increase significantly as the melt stream approaches the water pool surface. It is also shown that the measured temperature is between 551 and 557 degrees Kelvin at a location 1.1 meters above the water pool surface and between 545 and 565 degrees Kelvin at a location 0.6 meter above the water pool surface at time of MWC. The pressure increases from 5 to 5.2 Megapascals just before MWC (Figure 4) and the corresponding pressurization rate increases to 1.8 Megapascal per second during the first 0.4 second and then decreases to 1.5 Megapascal per second just before MWC (Figure 5). At pressures below 5.16 Megapascals, the water temperature

near the pool upper surface exceeds the saturation temperature. Flashing of the superheated water is not modeled in the analysis. This is expected to lead to an underestimate of the pressurization rate and pressure rise. Vaporization of water resulting from the absorption of thermal radiation in the water pool is modeled, however; this source of steam is assumed present when the pressure is below 5.16 Megapascals. At higher pressures, thermal radiation penetrating into the water pool is assumed to raise the water temperature without producing steam. This is expected to further underestimate the pressurization rate and pressure rise as some vaporization could still be induced by the radiant flux. The prefragmentation analysis calculated pressurization rate of 1.74 Megapascal per second compares well with the measured gas pressurization rate of 1.65 Megapascal per second at the time of MWC (Figure 5) though the measured pressure of 5.4 Megapascals is higher than the calculated pressure of 5.2 Megapascals (Figure 4). As discussed above, the pressure predicted by the model is expected to be an underestimate due to neglect of flashing from the water pool surface as well as vaporization of subcooled water by incident radiant heating.

For the Quenching Test 2, the calculated mixture temperature increases slowly during the first 0.2 second and then rises quickly from 536 to 547 degrees Kelvin when the melt stream approaches the water pool surface. From the measured gas-steam mixture temperature for Quenching Test 2, the temperature is between 538 and 545 degrees Kelvin at a location about 0.765 meter above the water pool surface at MWC. The pressure increases from the initial value of 5.80 to 6.06 Megapascals before MWC (Figure 6). The pressurization rate increases significantly after melt erosion begins at a time of 0.105 second and reaches 3.0 Megapascals per second before MWC (Figure 7). The calculated pressurization rate of 3.0 Megapascals per second at MWC is higher than the measured pressurization rate of 1.7 Megapascals per second (Figure 7).

2.3 Comparison of THIRMAL-1 with the Scoping Test

As noted earlier, the comparison of the THIRMAL-1 calculations of melt-water interactions with experiment data from FARO is dependent upon what is assumed about the prefragmentation of melt as it falls from the melt catcher to the water pool. The results of the preceding analysis that mechanistically models the partial breakup of the melt stream are therefore used to determine the conditions with which melt enters the water pool. Significantly, melt enters the water both as a melt stream and a surrounding mass of eroded droplets. A representation of the melt stream column assumed in the calculation at the first instant of water entry and illustrating the eroded droplets is provided in Figure 3.

For the Scoping Test conditions, 67 percent of the melt is eroded away in the form of melt droplets. About 73 percent of the eroded melt droplets (48 percent of the total released mass) are eroded from the stream prior to entry into the water pool. Only 27 percent of the eroded droplets (19 percent of the total released mass) are eroded away as the melt stream penetrates through the water pool. The remaining 33 percent of the melt is calculated to arrive as large segments created by breakup of the melt stream. These segments collect upon the bottom plate of the THERMOS vessel in a molten state. About 75 percent of the eroded melt droplets (50 percent of the total released mass) solidifies completely to form particles prior to collecting on the interaction vessel base. All of the remaining eroded droplets (17 percent of the total mass) are calculated to arrive in a partially frozen state. In particular, 70 percent or more of the heat of fusion is calculated to be removed for each of the partially frozen droplets.

If the partially frozen droplets are assumed to subsequently freeze as particulate entities, then the material collection is predicted to consist of 33 percent

of the released mass in a molten state and 67 percent as particles. This prediction is in excellent agreement with the state of material found at the bottom of the vessel in the experiment together with other predictions that are also in excellent agreement with the data (Table 1).

The calculated cumulative particle size distribution is given in Figure 8 together with the measured particle size distribution. This information is provided for fully solidified particles only, i.e., 50 percent of the total released melt for the calculation and 67 percent of the released melt for the Scoping Test. This figure provides the cumulative distribution in which the percentage of mass having a size less than a given diameter is plotted against that diameter. In general, a distribution of sizes is calculated by THIRMAL-1 as opposed to a single diameter reflecting the spatial and temporal variation in the local mechanisms and conditions under which droplet erosion occurs from the melt stream. In contrast, the prefragmentation analysis made the simplifying assumption of a single representative droplet diameter that was calculated to equal 5.5 millimeters. This representative particle diameter is used for the droplets that enter the water together with the melt stream. Consequently, it makes a significant and sharp contribution to the distribution at 5.5 millimeters. The calculated particle diameters range in size from 0.7 to 5.5 millimeters with a median size of 5.0 millimeters which compares very well with the measured median particle size of 4.5 millimeters.

The available data on melt quenching and steam formation from the Scoping Test are the time dependent pressure and temperature measured in the gas space overlying the water pool. Comparisons of the pressure calculated with THIRMAL-1 versus that measured during the experiment corresponding to the first 1.4 second following melt release are shown in Figures 4 and 5. The curves show two phases of pressurization: (i) a prefragmentation phase lasting approximately 0.46 second as the melt falls 1.83 meters from the release vessel to the upper surface of the water pool; and (ii) a melt-water interaction phase lasting about 1.0 second as the melt falls through the 0.87 meter deep water pool and collects at the bottom of the water pool. The first phase shows the effects of heating of the argon-steam cover gas mixture associated with the melt relocation in the gas space while the second phase includes the effects of steam generation in the water pool and further heating of the argon-steam mixture in the gas space. THIRMAL-1 does not model the long-term quenching of melt that collects and spreads over the base. Thus, the pressures calculated account only for fall stage melt quenching as the melt relocates downward through the water. However, the low rate of pressurization observed in the experiment over a longer timescale of 10 seconds indicates that pressurization due to the effects of heat transfer off of collected debris and melt is relatively unimportant during the melt fall stage. The virtual attainment of the peak pressure of 5.9 Megapascals at 0.8 second after melt entry into the water pool thus corresponds to essentially complete settling out of particles and droplets from the water pool. Prior to this time, the THIRMAL-1 calculated pressure increases more rapidly during the first 0.7 second. The calculated pressure increase rate during this interval shows excellent agreement with the measured pressure increase rate. The oscillation of the calculated pressurization rate after MWC is due to the limited number of Lagrangian particle groups used in the THIRMAL-1 input for the prefragmented melt droplets in the gas space. Increasing the number of particle groups used to represent the prefragmented melt droplets would reduce the magnitude of the oscillations. The predicted pressure is less than that in the test. However, as discussed earlier, this difference mainly represents an underestimate of the pressure rise during the prefragmentation phase due to neglect of flashing off of the top surface of the water pool. During the melt-water interaction phase, the pressure predicted with THIRMAL-1 tracks the measurement more closely. Here the pressurization is due to steam

formation from the melt-water interaction and provides a test of the modeling incorporated in the THIRMAL-1 code.

A more delicate test of the THIRMAL-1 models is provided by comparing the calculated and measured pressurization rates. Excellent agreement is obtained after the THIRMAL-1 calculation is initiated at the time of MWC (0.0 seconds on the figures). Between 0.7 and 0.8 second after nearly all of the pressure rise has been attained, the calculated pressurization rate is lower than the measurement. This may be a result of the assumption of a shorter melt release time of 0.207 second compared with 0.260 second noted by the experimenter. Another effect possibly contributing to this difference is the approximation in THIRMAL-1 of neglecting heat transfer from the debris on the bottom.

Overall, the pressure increase calculated with THIRMAL-1 agrees well with the pressure increase measured during the melt-water interaction phase. Specifically, a pressure increase of 0.7 Megapascal is calculated versus 0.7 Megapascal determined from the data. Thus, THIRMAL-1 is in excellent agreement with the data insofar as steam formation from melt-water interaction.

It is calculated that a net steam mass of 0.78 Kilogram exits the pool upper surface as the result of melt fall stage quenching. The net steam formation represents the removal of 2.5 Megajoules of enthalpy from the melt. A peak steam formation rate of 1.63 Kilogram per second at 0.5 second following melt entry into the pool is calculated. A rise in the pool water temperature of 4.4 degrees Kelvin is calculated by THIRMAL-1 corresponding to the removal of an additional 2.5 Megajoules of enthalpy from the melt. The combined enthalpy removal of 5.0 Megajoules represents the removal of 72 percent of the difference between the initial release melt enthalpy (at 2923 degrees Kelvin) and the melt enthalpy at the solidus temperature of 2848 degrees Kelvin. A rise of the argon-steam mixture temperature from 554 degrees Kelvin at MWC to 579 degrees Kelvin at 1.0 second following MWC is calculated by THIRMAL-1 that treats the cover gas as a control volume having a single temperature. The measured steam temperatures at various locations in the cover gas space are not uniform, especially soon after the melt stream enters the water. However, the various temperatures come to equilibrium at a temperature of 582 degrees Kelvin at about 5 seconds following MWC. The predicted temperature rise of 36 degrees Kelvin is in good agreement with the rise of 39 degrees Kelvin corresponding to the measured equilibrium value. The heatup here reflects in part the modeling of superheating of steam exiting the water pool due to heat transfer from melt as well as heat transfer from the prefragmented melt falling to the water surface.

2.4 Comparison of THIRMAL-1 with the Quenching Test 2

Conditions assumed for Quenching Test 2 and results obtained are shown in Table 1. It is predicted that 68 percent of the melt is eroded away in the form of melt droplets. About 67 percent of the melt droplets (45 percent of the total released mass) are eroded away from the melt stream prior to entering the water pool. Only 33 percent of the droplets (23 percent of the total released mass) are created as the melt stream penetrates through the water pool. The remainder of the melt is calculated to impinge as a stream (9 percent of the released mass) or arrive as large segments formed by large wave breakup (23 percent of the released mass) to collect upon the bottom in an initially molten state. Similar to the Scoping Test, all of the partially frozen droplets arrive at the pool bottom with over 70 percent of the heat of fusion removed. Thus, the THIRMAL-1 prediction of the corium collection state is in excellent agreement with the test results.

The calculated particle size distribution collecting upon the bottom plate in Figure 9 is compared with the measured particle size data. This information is provided for fully solidified particles only, that is, 46 percent of the total released melt for the calculation and 68 percent of the released melt for the Quenching Test 2. The calculated particle diameter ranges in size from 0.7 to 3.8 millimeters with a median size of 3.8 millimeter which is identical to the measured median particle size of 3.8 millimeters. This is also the representative eroded droplet diameter in the prefragmentation analysis for Quenching Test 2.

Comparison of the pressure calculated with THIRMAL-1 versus the measurement is shown in Figure 6. Thus, the calculated pressure accounts for fall stage melt quenching only. The pressure increase prior to MWC at 0.0 seconds has been calculated in the prefragmentation analysis. The pressure increase after MWC is calculated with THIRMAL-1. The attainment of a peak pressure of 7.5 Megapascals at 0.6 second after MWC is calculated while a peak pressure of 7.6 Megapascals at 0.75 second after MWC was measured. The pressure rise here reflects mainly steam generation from melt/water interaction and, to a lesser extent, cover gas heatup during the prefragmentation phase. The calculated and measured peak pressure rises are in excellent agreement.

The calculated pressurization rate is compared with that determined from the data in Figure 7. The trends of the calculated and measured pressurization rates are consistent. The measured pressure rise rate is lower than the THIRMAL-1 results prior to 0.45 second and higher than the THIRMAL-1 results after 0.45 second. A peak pressurization rate of 3.4 Megapascal per second at 0.35 second after MWC is calculated in very good agreement with the measured maximum rate of 3.3 Megapascals per second. The shift in time in the pressurization rate may again be a result of the assumption of a shorter melt release time of 0.26 second relative to the measured melt release time of 0.38 second.

It is calculated that a net steam mass of 2.18 Kilograms exits the pool upper surface as the result of melt fall stage quenching. This net steam formation represents the removal of 8.15 Megajoules of enthalpy from the melt. A peak steam formation rate of 8.5 Kilograms per second and steam temperature of 763 degrees Kelvin are calculated at 0.45 second following melt entry versus 11.0 Kilograms per second determined from the data assuming an equilibrium steam temperature at 573 degrees Kelvin. A rise in the water pool temperature of 3.5 degrees Kelvin is calculated by THIRMAL-1 corresponding to the removal of an additional 5.5 Megajoules of enthalpy from the melt due to fall stage quenching. The combined enthalpy removal of 13.6 Megajoules represents the removal of 64 percent of the difference between the initial released melt specific enthalpy at a temperature of 3023 degrees Kelvin and the melt specific enthalpy at the solidus temperature of 2848 degrees Kelvin.

An increase in the argon-steam cover gas mixture temperature from 550 degrees Kelvin at MWC to 607 degrees Kelvin (i.e., a 57 degree Kelvin rise) at 1.0 second following melt entry is calculated by THIRMAL-1. This is higher than the equilibrium gas-space temperature of 578 degrees Kelvin (a 28 degree Kelvin rise) obtained from the data about 4 seconds after MWC when the measured pressure decreased from the peak pressure of 7.6 to 7.2 Megapascal. The calculated gas space temperature exceeds the measured equilibrium temperature of 578 degrees Kelvin about 0.2 second after melt entry into the water pool and increases to 590 degrees Kelvin when all of the melt has entered the water at 0.3 second. Then, the calculated argon-steam temperature begins to slowly increase to the 607 degrees Kelvin. It is possible to speculate on why the cover gas temperature rise is overpredicted. Specifically, heat transfer between water droplets swept out of the mixing zone with steam and argon in the cover gas region is not modeled in THIRMAL-1. Such a heat transfer mode would tend to reduce the gas temperature. On

the other hand, heating of the cover gas due to heat transfer from swept out melt droplets and particles as well as superheated steam exiting the mixing zone are modeled.

An energy balance calculation was performed to evaluate the effects of water droplets swept out of the mixing zone on the gas space temperature. A gas space temperature rise of 35 degrees Kelvin is obtained which is in much better agreement with the measured increase in the equilibrium temperature of 28 degrees Kelvin.

When the water droplets are swept out of the mixing zone into the gas space region, the temperature difference between the gas-steam mixture and the water droplets causes heat to flow to the droplets. Further assessment of the amount of energy estimated to be transferred to the water droplets according to heat transfer rate considerations is consistent with the amount from the energy balance that provides good agreement with the measured gas space equilibrium temperature.

3. COMPARISON OF THIRMAL-1 WITH CCM EXPERIMENTS

3.1 Description of CCM Experiments

The CCM experiments are a set of six reactor material experiments performed at Argonne to obtain data on melt stream breakup in water, melt quenching, hydrogen generation, and debris formation [6]. The experiments were motivated by a need to better understand the interactions of corium melt with water inside the Three Mile Island Unit 2 lower plenum when about 20 tonnes of melt relocated from a crust-encased molten core pool onto the lower head. Of the six experiments, two were selected for comparison with THIRMAL-1 at the present time. These are the CCM-5 and CCM-6 tests (Table 2) in which 12 Kilograms of a 60 wt % UO_2 - 16 wt % ZrO_2 - 24 wt % stainless steel mixture was delivered into 1.07 meter deep pools of water at 0.117 and 0.114 Megapascal pressure. In CCM-5, the water pool was subcooled by 49 degrees Kelvin while in CCM-6, the water was very nearly saturated.

Comparison of THIRMAL-1 with data from the CCM tests is strongly motivated by the fact that the tests differ from FARO in several respects. First, the CCM experiments were performed at low pressures as is the case for melt-water interactions in the SBWR and AP600 as opposed to the high pressures of 5.0 Megapascals or greater characteristic of FARO. Second, one of the experiments employed water with a significant subcooling whereas the FARO tests were all conducted at low subcooling/near saturation conditions. This enables the code's capabilities to handle subcooling to be tested. Third, the melt has a significant metal phase constituent that gives rise to chemical oxidation reactions and hydrogen generation. Fourth, the experiments furnish data on the penetration of the melt leading edge through the water pool that can be used to compare with THIRMAL-1 predictions of the penetration of the stream leading edge as well as the envelope of the droplets and particles formed. Comparable data is not available from the FARO tests.

3.2 Comparison of THIRMAL-1 with the CCM-5 Experiments

A major difference between the low pressure CCM experiments and high pressure FARO tests is that prefragmentation of the melt stream does not occur in the CCM experiments because of the lower density of the gas-steam mixture and the short fall height. There is negligible heating or pressurization of the cover gas mixture prior to melt/water contact. Thus the THIRMAL-1 calculations for the CCM experiments assume that all of the released melt enters the water as a circular melt stream.

TABLE 2. Comparison of the THIRMAL-1 Code with the Results of the CCM-5 and CCM-6 Experiments

CCM Test Conditions	CCM-5		CCM-6	
Water pool depth, m	1.07		1.07	
Initial water subcooling, K	49		2.5	
Gas composition, mole %	17 % Steam + 83%[a] Ar		96 % Steam + 4%[a] Ar	
Gas volume, m^3	0.46		1.14	
Gas temperature, K	363		404	
Pressure, MPa	0.117		0.114	
Melt composition, wt %	60% UO_2 + 16% ZrO_2 + 24% SS (67% Fe + 21% Cr + 12% Ni)			
Initial melt superheat, K	157		157	
Released melt mass, Kg	10.87		11.34	
Diameter at release vessel nozzle, cm	50.8		50.8	
Free Fall Distance in gas, cm	34		34	
Thermite vessel pressure at onset of melt release, MPa	0.117		0.202	
Comparison of THIRMAL-1 Predictions and Exp. Data	**Experiment**	**Prediction**	**Experiment**	**Prediction**
Corium collection conditions, wt% particles/droplets/stream	100/0/0	53/47[a]/0	100/0/0	50/48[a]/2
Fine fragments (<1.70 mm), Kg (wt%)	1.875 (17)	2.482 (23)	3.02 (27)	5.2 (46)
Intermediate-size fragments				
(1.7< <3.36 mm), Kg (wt %)	2.57 (24)	3.27 (30)	2.32 (21)	1.2 (10)
(3.36 < <6.35 mm), Kg (wt %)	2.088 (19)	2.05 (19)	2.36 (20)	1.10 (10)
Large fragments (> 6.35 mm), Kg (wt %)	4.347 (40)	3.08 (28)	3.7 (32)	3.9 (34)
Median particle size, mm	5.0	6.0	3.8	2.0
Melt and bottom plate contact after melt entry into water, s	0.95	0.81	0.29	0.27
Mean velocity of melt in water, m/s	1.1	1.3	3.7	4.0
Maximum pressure reached during fall stage quenching, MPa	0.246	0.256	0.354	0.304
Gas-steam temperature at time of maximum pressure occurrence, K	390	388	417	411
Hydrogen mass formed, g	24.7	28.4	47.2	56.7
Total steam generated, g	306	342	1423	1134

a) Includes partially frozen droplets.

The CCM-5 experiment was performed with subcooled water at an initial temperature of 328 degrees Kelvin equivalent to 49 degrees Kelvin of subcooling. The melt stream release and entry water pool conditions calculated for CCM-5 and 6 are summarized in Table 2 that also compares the THIRMAL-1 predictions with the experiment results.

Figure 10 shows the calculated time dependent penetration of the melt stream leading edge and the penetration front of the eroded droplets and particles together with the times of response indications of thermocouples located at various distances beneath the water surface in the path of the melt. The melt stream leading edge is calculated to penetrate to a depth of 0.24 meter during the first 0.1 second following entry into the water pool and then vary in an oscillatory manner from 0.1 second to 0.4 second. The oscillations are a result of breakup of the melt stream immediately behind the leading edge when the amplitude of unstable long waves along the stream column exceeds the size of the melt stream. At 0.4 second following entry into the water, the melt stream breakup distance is calculated to increase with time owing to an increase in the vapor volume fraction surrounding and below the melt stream. At 0.64 second following entry into the water (0.80 second after melt release), the melt stream leading edge has penetrated downward through approximately half the water pool depth. The melt stream breakup distance is calculated to decrease thereafter owing to a reduced melt stream entry velocity and diameter corresponding to the decreasing melt release rate. The location of the droplet/particle penetration front is calculated to first reach the base at 0.81 second following entry into the water. This corresponds to a mean melt velocity in the water pool of 1.3 meter per second.

As the corium penetrated through the water, it contacted thermocouples or was at least in close enough proximity to thermocouples to produce responses. Thermocouples that exceeded 1400 degrees Centigrade indicative of contact with corium are indicated by the shaded circles or squares. The axial centerline thermocouples clearly show a significant decrease in the melt penetration velocity after 0.1 second following melt entry into the water pool. This is indicative of a change in the melt configuration from a rapidly penetrating stream to slower penetrating droplets and particles implying breakup of the stream at a distance less than 0.31 meter. This distance is equivalent to 9 melt stream entry diameters.

Other thermocouples showed responses but these were significantly less than a rise to 1400 degrees Centigrade (representative of thermocouple melting) or more. For example, a rise of 100 or 200 degrees Kelvin would fall into this category. Such thermocouples are denoted with open circles on Figure 10. Responses of this nature are consistent with thermocouples being heated by heat transfer from droplets and particles as opposed to being engulfed by a melt stream. Finally, the squares correspond to thermocouples located on the base of the water pool at radii of 5.08 centimeters with shaded and open having the same meaning.

The predicted time dependent leading edge penetrations of the melt stream as well as eroded droplets and particles are both in excellent agreement with the stream and droplet front penetrations obtained from the thermocouple responses. Also the predicted time at which melt contacts the base is in very good agreement with the arrival times obtained from thermocouples on and near the base. The high temperatures measured at the base are consistent with material collection and agglomeration upon the base. The measured time of 0.95 second for corium to reach the thermocouples on the vessel bottom section is a little longer than the THIRMAL-1 calculated melt settling time of 0.81 second.

Seventy percent of the melt is calculated to be eroded in the form of melt droplets due to the effects of Kelvin-Helmholtz instability-induced stripping along the

melt stream column as well as droplet formation by boundary layer stripping from the rear of the leading edge of the melt stream. The remaining 30 percent of the melt is calculated to form large melt stream segments from breakup of the melt stream at the leading edge due to large wave instability. About 76 percent of the eroded melt droplets (53 percent of total released melt mass of 10.83 Kilograms) solidify completely to form particles prior to collecting on the bottom of experiment vessel. About 8 percent of the fully solidified particles (5 percent of the total released mass) is metallic melt. Nine percent of the eroded melt (6 percent of the total released mass) is calculated to arrive in a partially frozen state (above 70 percent heat of fusion removed). Thus, the material accumulating at the bottom is calculated to consist of solid particles, nearly solidified droplets, and 41 percent of the released melt mass that arrives in a molten state. About 19 percent of the total released melt mass arriving on the floor is metallic molten droplets. These results are included in Table 2. The THIRMAL-1 calculated debris size distribution collecting upon the base is shown in Figure 11 and compared with the measured particle size distribution. Upon posttest examination, melt arriving on the floor in a molten state was largely agglomerated together with solidified particles. The debris was sieved through 6350, 3360, and 1700 micron screens. Agglomeration effects raise the question of what portion of the debris was actually sized in arriving at the measured size distribution. For this reason, three different calculated size distributions representing different portions of the droplets and particles formed are plotted in Figure 11. The calculated diameter for the melt/droplet/segment distributions range in size from 0.7 to 16.0 millimeters with a median size of 2.8 millimeters. The calculated median diameter for fully solidified particles is 6.0 millimeters and the calculated median diameter for the 70 percent or greater solidified particle size distribution is 4.0 millimeters.

Data on transient melt quenching and steam formation behavior are the time dependent pressure and temperature measured in the gas space overlying the water pool. Comparison of the pressure calculated with THIRMAL-1 versus that measured in the experiment during the first 1.7 seconds following melt release is shown in Figure 12. For 0.16 second before melt/water contact as evidenced by thermocouple response, the data shows a small pressure rise. The pressure calculated with THIRMAL-1 accounts only for fall stage melt quenching as the melt relocates downward through the water pool. In addition, THIRMAL-1 does not model the long-term quenching of melt that collects and spreads over the water pool base. The virtual attainment of the peak pressure soon after melt entry into the water pool corresponds to essentially the complete settling out of particles and droplets from the water pool. The calculated pressure increases more slowly during the first 0.3 second after melt entry into the water pool than the CCM-5 data. THIRMAL-1 neglects heating of steam-gas mixture and steam generation associated with the melt stream relocation behavior as the melt stream falls through the gas space. The calculated pressure increase rate is slightly higher than the measured pressure increase rate between 0.4 and 0.85 second. This could reflect steam condensation on the dispersed subcooled liquid droplets swept away by the steam flow out of the mixing zone. This condensation process in the gas space is not modeled. The mixing zone regime flow become highly dispersed droplet flow at 0.3 seconds following melt entry into the water pool consistent with this latter conjecture. A peak pressure of 0.26 Megapascal (i.e., 0.14 Megapascal of pressure increase) is calculated versus a measured peak pressure 0.25 Megapascal (i.e., 0.13 Megapascal of pressure increase).

A peak steam formation rate of 0.35 Kilogram per second is calculated at 0.5 second following melt entry. The steam formation rate includes steam converted into hydrogen by oxidation of metal. The masses of steam and hydrogen generated and predicted by THIRMAL-1 are compared with those determined from the data in Table 2. The analysis of hydrogen generation is based upon mass spectrometry of gas samples

extracted shortly after the test. The investigation of the steam generation was focused on the short-term quenching of the corium, i.e., during the melt stream fall stage, rather than any long-term debris cooling stage. The steam generation during the melt stream fall stage is determined from the experiment vessel pressurization data in the test that were analyzed along with the amount of hydrogen generated. It is determined that a total hydrogen mass of 25 grams (or 12 gram-moles) was generated in the CCM-5 test. Therefore, a total steam mass of 306 grams is determined based on the maximum experiment vessel pressure of 0.246 Megapascal and the corresponding gas-steam mixture temperature of 390 degrees Kelvin. In the THIRMAL-1 analysis, a total steam mass of 342 grams and a hydrogen mass of 28 grams are calculated to exit the water pool surface as the result of melt fall stage quenching. These predictions are in good agreement with the experiment values. The time dependent gas-steam mixture temperature increases from 363 to 388 degrees Kelvin during the first 1.5 seconds following melt entry into the water pool. This calculated temperature increase compares well with the temperature increase measured by the thermocouple located 46 centimeters above the water surface which rose from 363 to 390 degrees Kelvin at the time of maximum pressure.

3.3 Comparison of THIRMAL-1 with the CCM-6 Experiment

The CCM-6 experiment was conducted with nearly saturated water at 374 degrees Kelvin (2.5 degrees Kelvin of subcooling). Figure 13 shows the calculated time dependent penetration of the melt stream leading edge and the melt droplet/particle penetration front as well as the thermocouple response indications. The melt stream leading edge is calculated to quickly penetrate to the base of the pool after only 0.27 second. Droplets and particles are calculated to first reach the base only slightly sooner. This corresponds to a mean melt penetration velocity through the water of 4.0 meters per second. Contact with the base was indicated by a thermocouple 5.08 centimeters away from the centerline at 0.29 second. The predicted leading edge penetration is in excellent agreement with the melt stream penetration inferred on the basis of major thermocouple responses (i.e., increases in temperature readings exceeding 1400 degrees Centigrade). The thermocouples also indicate a rapid penetration of the stream to at least 0.85 meter depth.

Sixty-six percent of the melt is calculated to be eroded as droplets due to Kelvin-Helmholtz instability-induced stripping along the melt stream column as well as droplet formation by boundary layer stripping from the rear of the leading edge. The remaining 34 percent of the melt is calculated to impinge as a stream (2 percent of the total released mass of 11.4 Kilograms) or arrive as large melt stream segments (32 percent of the total released mass) due to breakup of the melt stream upon the bottom plate of the experiment vessel. About 62 percent of the eroded melt droplets (41 percent of total released melt mass of 11.4 Kilograms) solidifies completely to form particles prior to collecting on the bottom of experiment vessel. Five percent of the eroded melt (3 percent of the total released mass) is calculated to arrive in a partially frozen state (above 70 percent heat of fusion removed). Twenty-eight percent of the large segments are calculated to arrive in a solidified state. Thus, the material accumulating at the bottom is calculated to consist of solid particles, nearly solidified droplets and 47 percent of the released melt mass that arrives in a molten state. These results are included in Table 2. Note that the large segments are included with droplets and particles in Table 2.

The calculated debris size distribution collecting upon the base is taken to be that for all droplets and particles formed either by Kelvin-Helmholtz-induced stripping, boundary layer stripping, or large wave breakup. The calculated diameters range in size from 0.6 to 27 millimeters with a median size of 2.0 millimeters which is below the measured median particle size of 3.8 millimeters. Distributions of fully solidified

particles of combined partially and fully solidified droplets and particles were not calculated.

Comparison of the pressure calculated with THIRMAL-1 versus that measured in the experiment during the first 1.6 seconds following melt release is shown in Figure 14. The calculated pressure increase is lower than the CCM-6 data during the first 0.2 second after melt release. The calculated pressure increase is comparable with the measured pressure increase thereafter. A peak pressure of 0.3 Megapascal (i.e., a 0.19 Megapascal pressure increase) is calculated versus a measured peak pressure of 0.35 Megapascal (i.e., 0.24 Megapascal of pressure increase).

A peak steam formation rate of 2.5 Kilograms per second at 0.28 second following melt entry into the water pool is calculated and a net steam generation rate of 2.3 Kilograms per second at 0.28 second following MWC. The net steam generation rate is approximately equal to the steam formation rate after 0.4 second. This is consistent with termination of the oxidation of metallic melt in the continuous vapor flow. The mass of steam and hydrogen predicted by THIRMAL-1 and those determined from the data are shown in Table 2.

In order to obtain the experiment steam generation during the fall stage, the experiment vessel pressurization data in the test was analyzed along with the amount of hydrogen generation determined from analysis of the gas samples. It was determined that a total hydrogen mass of 47 grams (or 23 gram-moles) was generated. Therefore, a net steam mass of 1014 grams (or a total of 1423 grams of steam formation) is estimated based on the maximum experiment vessel pressure of 0.354 Megapascal and the corresponding gas-steam mixture temperature of 417 degrees Kelvin. In the THIRMAL-1 analysis, a net steam mass of 625 grams (or a total steam mass formation of 1134 grams) and a hydrogen mass of 57 grams are calculated as the result of melt fall stage quenching.

The calculated time dependent gas-steam mixture temperature that increases from 404 to 411 degrees Kelvin during the melt fall stage. This calculated temperature increase is lower than the measured temperature rise from 404 to 417 degrees Kelvin at the time of maximum pressure.

4. SUMMARY OF FINDINGS

THIRMAL-1 calculations were found to be in excellent agreement with the results of the Ispra FARO Scoping Test and Quenching Test 2 as well as the ANL CCM-5 and CCM-6 experiments.

A mechanistic model for prefragmentation in the FARO apparatus was developed and applied to both the Scoping Test and Quenching Test 2. The melt configuration that is predicted to enter the water differs significantly from that assumed by Angelini, Yuen, and Theofanous [10]. In particular, the melt does not enter the water fully fragmented as a cloud of spheres. Instead, the melt is calculated to enter as a reduced diameter stream surrounded by melt droplets eroded from the stream surface by the growth of Kelvin-Helmholtz instabilities. Instability growth and erosion are effective in the FARO apparatus due to the high gas densities prevalent at the high pressures (e.g., 5.0 Megapascals) at which the FARO tests are carried out combined with the long fall heights from the melt release vessel to the water surface (about 1.8 meters). The eroded droplets heat up the cover gas above the water surface by thermal radiation and forced convection heat transfer. The calculated pressurization during the prefragmentation stage is in good agreement for the Quenching Test 2 but underpredicted for the Scoping Test. In the latter case, the difference may be attributed to flashing of steam off

of the surface of the water pool. Flashing in this manner would not be a factor in Quenching Test 2 or in advanced reactor systems. The results of the prefragmentation analysis are used to provide THIRMAL-1 with the conditions with which the reduced diameter stream and eroded droplets enter the surface of the water pool.

For both FARO tests, the calculated pressurization rate from steam formation is in excellent agreement with that determined from the data. The calculated time for melt to penetrate downward through the water pool is also in excellent agreement with that inferred from thermocouple responses indicative of interaction with melt near the top and bottom of the water pool. These results lend confidence to the modeling of melt stream penetration and breakup by various instability mechanisms that determine the amount and sizes of droplets formed as well as the modeling of multiphase heat transfer and flow inside the mixing zone that determine the net rate of steam formation. The predicted debris size distribution also agrees very well with that measured in posttest examination. This lends further confirmation to the modeling of melt breakup by Kelvin-Helmholtz instabilities that produces droplets of the observed sizes during both the prefragmentation and melt-water interaction phases.

The only notable discrepancy between the THIRMAL-1 calculations and the FARO data concerns the gas space temperature rise in Quenching Test 2 that is significantly overpredicted. The difference here was shown to correspond to the neglect in THIRMAL-1 of the cooling effects of water droplets swept out of the mixing zone into the overlying gas space. In particular, it was shown through a standalone energy balance analysis that the droplets constitute more than a sufficient heat sink to account for the discrepancy. Interaction with half of the swept out water mass would bring the calculated and measured gas space temperatures into agreement while the remaining half of the droplets deposit upon the walls and structures in the gas space. A separate standalone estimate of energy transfer rates from the gas space to the interacting water droplets further supports this explanation of the discrepancy. Thus, modeling for the interactions of swept out water droplets is identified as a worthwhile addition to THIRMAL-1 for future comparisons with the ongoing FARO tests.

For CCM-5 and CCM-6, the THIRMAL-1 predictions of the time dependent penetration of the melt stream leading edge and droplet/particle penetration front are in excellent agreement with the locations indicated by the timing of responses from thermocouples located along the experiment vessel centerline in the path of the melt or off the centerline on the base at the bottom of the water pool. This lends a high level of confidence to the modeling of melt stream breakup by three mechanisms: (i) Kelvin-Helmholtz (i.e., small wave) instabilities along the melt stream column, (ii) boundary layer stripping from the rear of the initial penetrating leading edge, and (iii) large wave breakup of the leading edge. For CCM-5, the code predicts an increase in the leading edge penetration when a large amount of vapor has been created in the mixing zone as observed in the penetration data confirming the instability modeling that depends upon the conditions in the surrounding medium. The very good agreement with the pressurization data from steam formation lends confidence to both the modeling of melt stream breakup and the sizes of droplets formed as well as multiphase flow and heat transfer in the mixing zone. The modeling approach here is further confirmed by the good agreement between the predicted and measured debris particle sizes. Very good agreement is obtained for the amount of hydrogen produced supporting the modeling of oxidation of droplets of the metallic constituent by interaction with flowing steam in the mixing zone.

ACKNOWLEDGEMENTS

This work was sponsored by the United States Department of Energy Advanced Reactor Severe Accident Program. The authors are indebted to S. W. Sorrell, ARSAP Program Manager and S. L. Additon (TENERA). The authors also appreciate the efforts of L. M. McUmber (ANL/RE) in providing original data from the CCM experiments. Argonne project management was provided by L. Baker, Jr. The manuscript was typed by L. J. Ondracek and J. A. Wozniak (ANL/RE).

NOMENCLATURE

A_J' = melt stream surface over which melt erosion occurs, m^2
a = melt stream radius, m
a_g = absorption coefficient of steam-gas mixture, 1/m
a_m = absorption coefficient of multiple melt droplets/particles, 1/m
= $1.5\ \epsilon_m\ \alpha_p/\bar{D}_p$
C_{rad} = the fraction of radiation heat transfer absorbed by the gas-steam mixture, ~0.4
$\bar{D}_p$ = representative eroded melt droplet diameter, m
D_h = test vessel diameter, ~ 0.46 (ST) and 0.74 (QT2) meters
D_J = melt stream diameter, m
$\bar{D}_J$ = average melt stream diameter, $\approx (D_{J,0} + D_{J,e})/2$, m
$D_{J,e}$ = melt stream diameter at the water pool surface, m
$D_{J,0}$ = melt stream diameter at the location where melt erosion begins, m
F = absorbed fraction in an infinite medium
f = subscript denoting properties evaluated at the film temperature, T_f
H_{fall} = melt stream fall distance before MWC, m
h_{conv} = force convection heat transfer coefficient, W/(m²·K)
= $k_f/\bar{D}_p\ \left(2.0 + 0.6\ Re_p^{0.5}\ Pr_f^{0.3334}\right)$,
h_{rad} = radiation heat transfer coefficient, W/(m²·K)
= $\epsilon_m\ \sigma_B\ \left(T_m^4 - T_{sat}^4\right)/\left(T_m - T_{sat}\right)$
k_{max} = wavenumber corresponding to the maximum wave growth rate, 1/m
L_m = mean free length, ~ 0.5 D_h, m
Pr_f = Prandtl number, $C_f\ \mu_f/k_f$
Re_p = melt droplet Reynolds number, $\bar{U}_J\ \bar{D}_p\ \rho_f/\mu_f$
T_f = film temperature, ½ $(T_g + T_m)$, K
T_g = gas-steam mixture temperature, K
T_m = melt temperature, K
t_o = time period corresponding to the melt stream fall distance, x_o, s
T_{sat} = saturation temperature, K
U_J = melt stream velocity, m/s
$U_{J,min}$ = minimum required stream velocity, m/s
$\bar{U}_J$ = average melt stream velocity for melt erosion, m/s
$\approx (H_{fall} - x_o)/(t_{fall} - t_o)$,
x_o = melt stream fall distance when the initial disturbance on the melt stream surface reaches the critical unstable wave magnitude, λ_{max}, and melt erosion begins, m
x_1 = free fall distance at the leading edge of melt stream, m
σ_m = melt surface tension, N/m
σ_B = Stefan-Boltzman constant, $5.67 \cdot 10^{-8}$ W/(m²·K)
ρ_f = gas mixture density surrounding the melt stream evaluated at the film temperature, T_f, Kg/m³
ρ_m = melt density, Kg/m³

λ_{max} = wavelength corresponding to the maximum wave growth rate, m
η (t) = unstable wave magnitude at time t, m
η_o = initial disturbance magnitude, m
ϵ_m = melt emissivity
ϵ_w = steel wall emittance
α_p = melt droplet/particle volume fraction in the cover gas space
α_{max} = maximum wave growth rate due to Kelvin-Helmholtz (K-H) instability, 1/s

REFERENCES

[1] C. C. Chu, J. J. Sienicki, and B. W. Spencer, "The THIRMAL-1 Computer Code for Analysis of Interactions Between a Stream of Molten Corium and a Water Pool-Volume 1, Code Manual," EPRI Report, EPRI TR-103417-V1 (December 1993).

[2] C. C. Chu, J. J. Sienicki, and B. W. Spencer, "The THIRMAL-1 Computer Code for Analysis of Interactions Between a Stream of Molten Corium and a Water Pool-Volume 2, User's Manual," EPRI Report, EPRI TR-103417-V2 (December 1993).

[3] J. J. Sienicki, S. K. Wang, and B. W. Spencer, "Analysis of Melt Arrival Conditions on the Lower Head in U. S. LWR Configurations," NURETH-5, 2 (1992).

[4] J. J. Sienicki, C. C. Chu, B. W. Spencer, W. Frid, and G. Löwenhielm, "Ex-Vessel Melt Coolant Interactions in Deep Water Pool: Studies and Accident Management for Swedish BWRs," CSNI Specialists Meeting on Fuel-Coolant Interactions, Santa Barbara, CA, January 5-8, 1993, NUREG/CP-0127, NEA/CSNI/R(93)8, p. 37 (1994).

[5] D. Magallon and H. Hohmann, "High Pressure Corium Melt Quenching Tests in FARO," CSNI Specialists Meeting on Fuel-Coolant Interactions, Santa Barbara, CA, January 5-8, 1993, NUREG/CP-0127, NEA/CSNI/R(93)8, p. 1 (March 1994).

[6] B. W. Spencer, S. K. Wang, C. A. Blomquist, L. M. McUmber and J. P. Schneider, "Fragmentation and Quench Behavior of Corium Melt Streams in Water," NUREG/CR-6133, ANL-93/32 (February 1994).

[7] B. W. Spencer, J. D. Gabor, J. C. Cassulo, and D. J. Kilsdonk, "Results of Scoping Experiments on Melt Stream Breakup and Quench," International ANS/ENS Topical Meeting on Thermal Research Safety, 1, p. II.8-1 (1986).

[8] B. W. Spencer, J. D. Gabor and J. C. Cassulo, "Effect of Boiling Regime on Melt Stream Breakup in Water," Particulate Phenomena and Multiphase Transport, 3, ed. T. N. Veziroglu, Hemisphere Publishing Co. (1987).

[9] J. P. Schneider, M. Marciniak and B. G. Jones, "Breakup of Metal Jets Penetrating a Volatile Liquid," NURETH-5, 2, 437-449 (1992).

[10] S. Angelini, W. W. Yuen and T. G. Theofanous, "Premixing-Related Behavior of Steam Explosion," CSNI Specialists Meeting on Fuel-Coolant Interactions, Santa Barbara, CA, January 5-8, 1993, NUREG/CP-0127, NEA/CSNI/R(93)8, p. 99 (1994).

[11] M. Bürger, S. H. Cho, E. V. Berg, and A. Schatz, "Breakup of Melt Jets as Precondition for Premixing: Modeling and Experimental Verification," CSNI Specialists Meeting on Fuel-Coolant Interactions, Santa Barbara, CA, January 5-8, 1993, NUREG/CP-0127, NEA/CSNI/R(93)8, p. 54 (March 1994).

[12] C. C. Chu and M. L. Corradini, "One-Dimensional Transient Fluid Model for Fuel-Coolant Interaction Analysis," Nucl. Sci. and Eng. 101, 48-71 (1989).

[13] B. J. Meister and G. F. Scheele, "Prediction of Jet Length in Immiscible Liquid Systems," AICHE Journal 15, No. 5, p. 689 (1969).

[14] D. W. Condiff, D. H. Cho, and S. H. Chan, "Heat Radiation Through Steam in Direct Containment Heating," Trans. Am. Nucl. Soc., 53, p. 561 (1986).

[15] C. L. Tien, "Thermal Radiation Properties of Gases," Advances in Heat Transfer, 5, ed. T. F. Irvine, Jr. and J. P. Hartnett, Academic Press, New York (1968).

[16] D. W. Condiff, Private Communication, Argonne National Laboratory (January 1994).

[17] K. H. Sun, J. M. Gonzalez, C. L. Tien, "Calculations of Combined Radiation and Convective Heat Transfer in Rod Bundles Under Emergency Cooling Conditions," ASME Journal of Heat Transfer 98, p. 414 (1976).

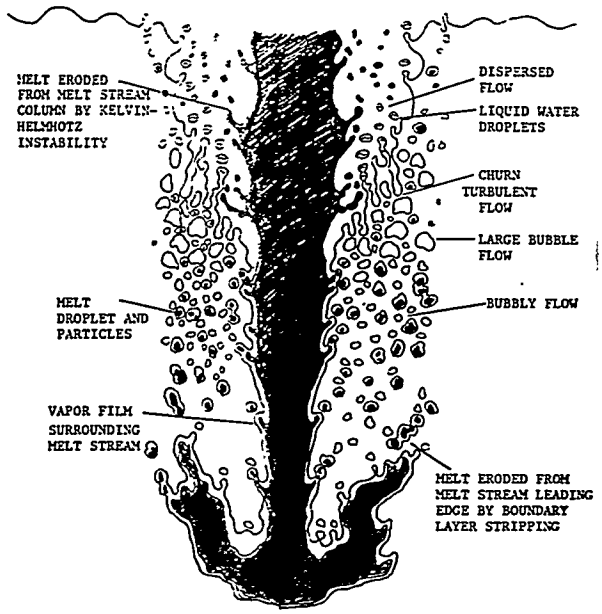

Figure 1. Depiction of melt stream penetrating through a water pool.

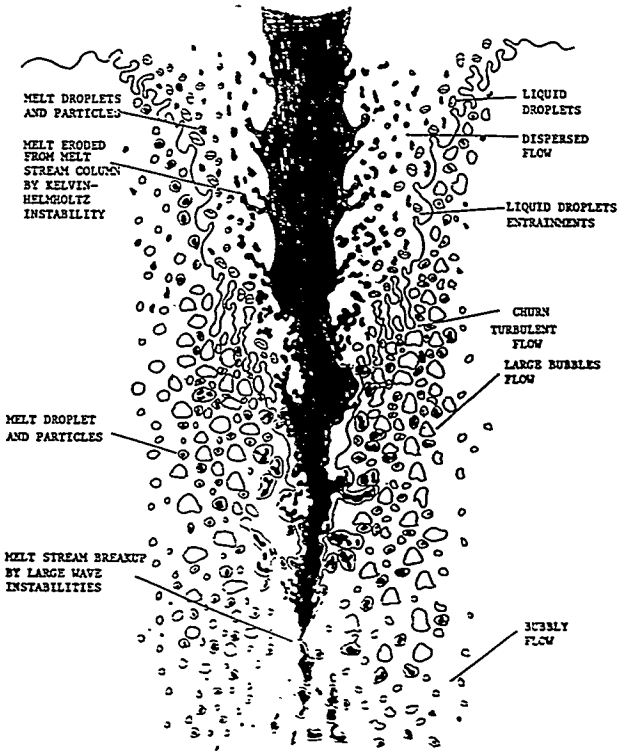

Figure 2. Depiction of erosion and breakup of melt stream in a water pool.

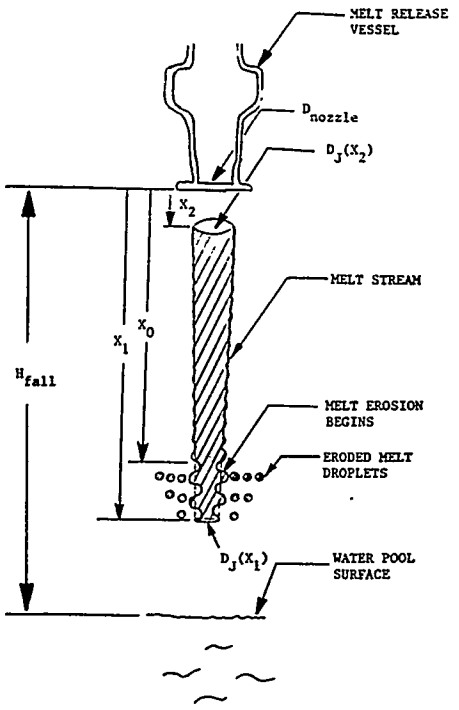

Figure 3. Depiction of prefragmentation analysis for the FARO Tests.

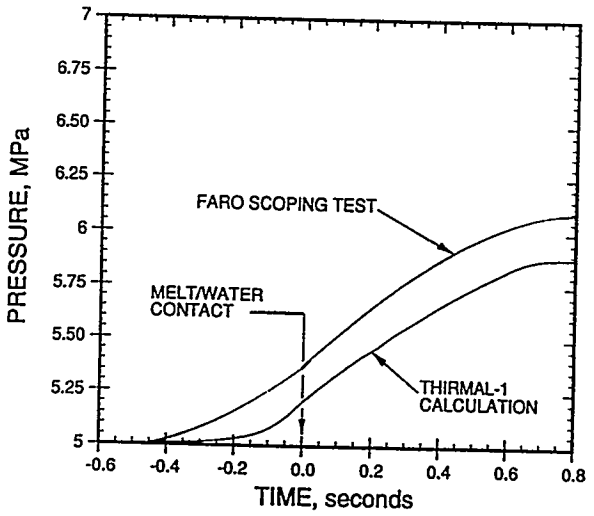

Figure 4. Vessel pressure increase for FARO Scoping Test.

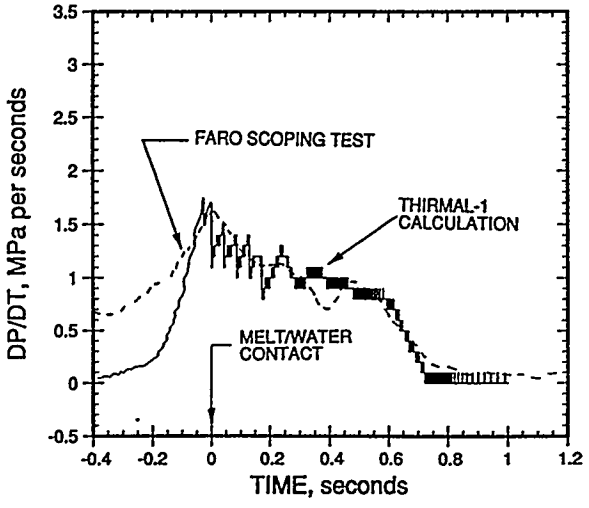

Figure 5. Vessel pressure increase rate for FARO Scoping Test.

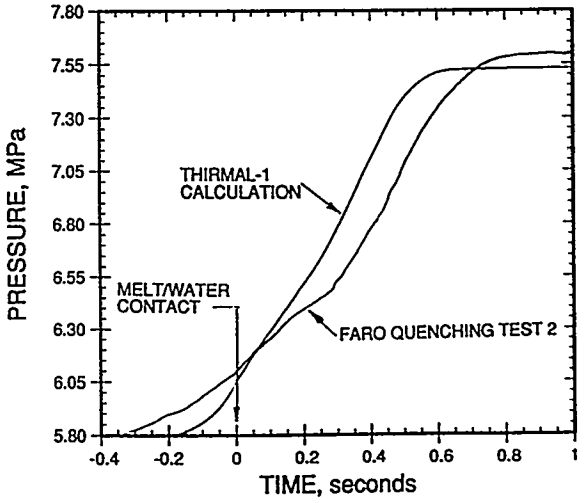

Figure 6. Vessel pressure increase for FARO Quenching Test 2.

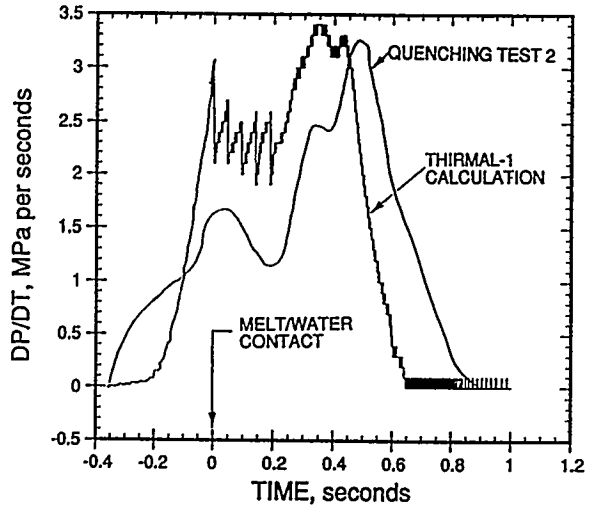

Figure 7. Vessel pressure increase rate for FARO Quenching Test 2.

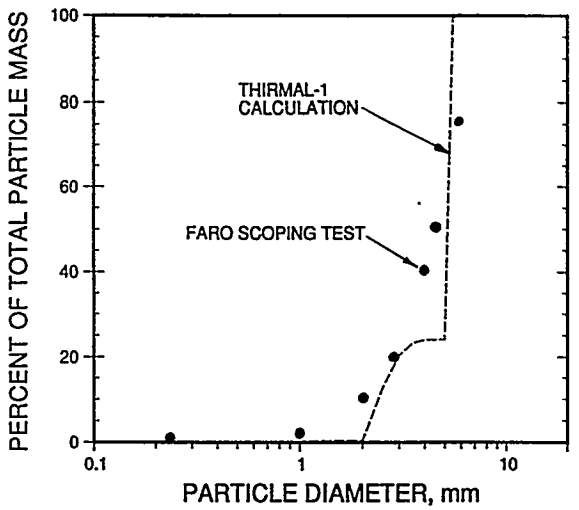

Figure 8. Cumulative particle size distribution for FARO Scoping Test.

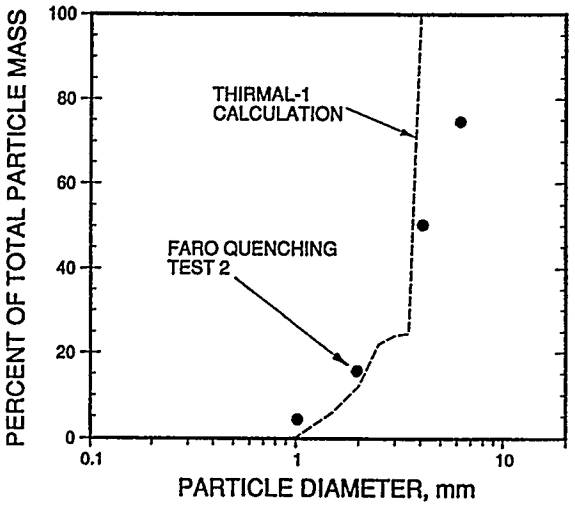

Figure 9. Cumulative particle size distribution for FARO Quenching Test 2.

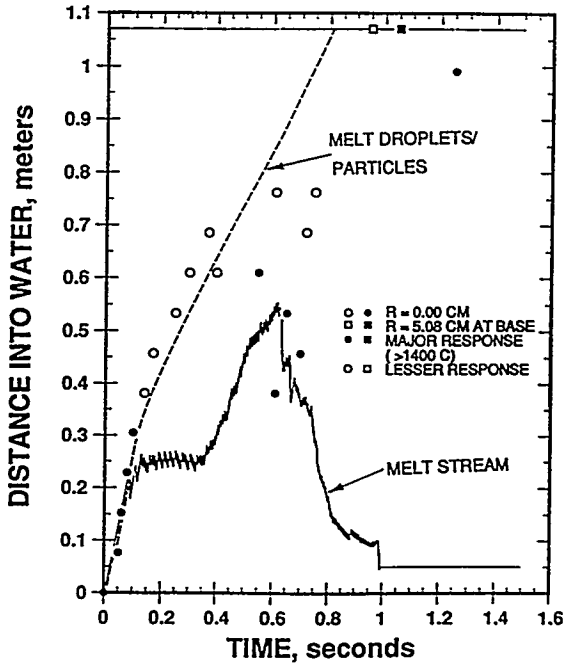

Figure 10. Comparison of THIRMAL-1 calculated penetration of melt stream and melt droplet/ particle leading edge with thermal responses of thermo-couples for CCM-5 experiment.

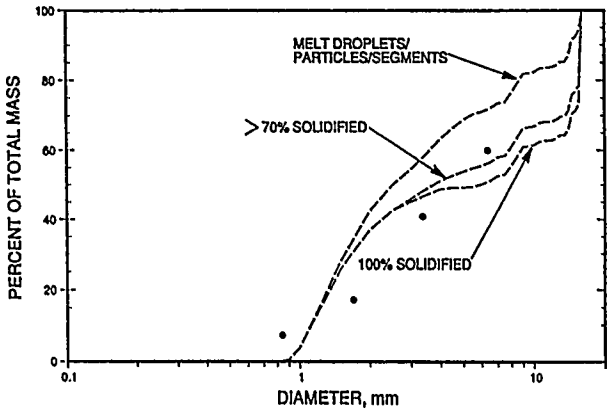

Figure 11. Comparison of THIRMAL-1 calculated cumulative particle size distribution with posttest debris size data for CCM-5.

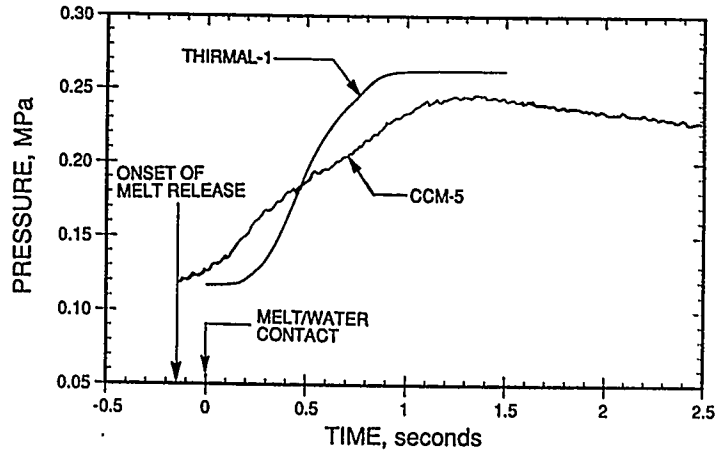

Figure 12. Comparison of THIRMAL-1 calculated experiment vessel pressure increase with measured pressure data for CCM-5 experiment.

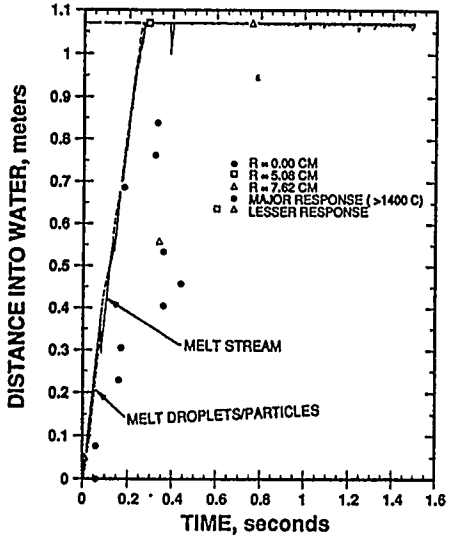

Figure 13. Comparison of THIRMAL-1 calculated penetration of melt stream and melt droplet/particle leading edge with thermal responses of thermocouples for CCM-6 experiment.

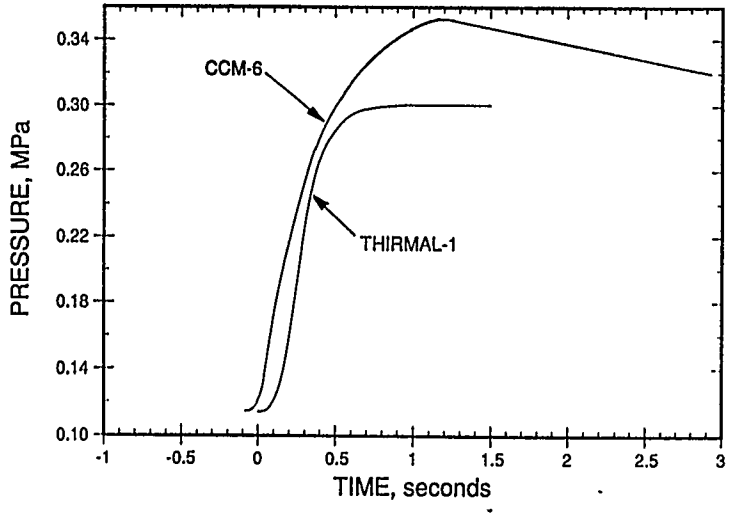

Figure 14. Comparison of THIRMAL-1 calculated experiment vessel pressure increase with measured pressure data for CCM-6 experiment.